Interaction between Inertia, Viscosity and Elasticity in Soft Robotic Actuator with Fluidic Network

Benny Gamus, *Member, IEEE,* Lior Salem, *Member, IEEE,* Eran Ben-Haim, *Member, IEEE,* Amir D. Gat, *Member, IEEE,* and Yizhar Or, *Member, IEEE*

***Abstract*—Soft robotics is an emerging bio-inspired concept of actuation, with promising applications for robotic locomotion and manipulation. Focusing on actuation by pressurized embedded fluidic networks, existing works examine quasistatic locomotion by inviscid fluids. The current work presents analytic formulation and closed-form solutions of an elastic actuator with pressurized fluidic networks, while accounting for the effects of solid inertia and elasticity, as well as fluid viscosity. This allows modelling the system's step-response and frequency response as well as suggesting mode elimination and isolation techniques. The theoretical results describing the viscous-elastic-inertial dynamics of the actuator are illustrated by experiments. The approach presented in this work may pave the way for the design and implementation of soft robotic legged locomotion that exploits dynamic effects.**

I. Introduction

Soft robotics is a bio-inspired field of study which introduces a new concept of robotic design with high compliance. Though there is no clear boundary to the defenition of a soft robot, continuous actuation and deformation, rather than a conventional chain of rigid links with discrete actuation at the joints, is often described as a key component [1], [2], [3]. Soft robots have advantages in negotiating unstructured environments, adapting to complex terrain and interacting with humans and delicate objects, and show promise for medical applications.

The actuation of an elastic continuous structure involves increased kinematic and dynamic complexity [4]. The main approaches include dielectric elastomeric actuators (DEAs) [5], which deform the soft body by electrostatic forces; shape memory alloy (SMA) [6], [7] which strain under heating; tendons manipulating rigid fixtures, from hard continuum elephant trunk [8] to a soft octopus-inspired arm [9]; pneumatic artificial muscle (PAM) actuators, also known as McKibben muscle [10], often used to manipulate rigid structures [11], and embedded fluidic network (EFN) (often referred to as fluidic elastomer actuators). The latter, which is the focus of this work, consists of a fluid-filled network of cavities, embedded into the soft body. Fluid pressurization creates inflation of the embedded cavities, which, combined with asymmetry, creates a deflection of the elastic structure in a desired way.

Benny Gamus, Eran Ben-Haim, Amir D. Gat and Yizhar Or are with the Faculty of Mechanical Engineering, Technion – Israel Institute of Technology, Technion City, Haifa, Israel 3200003.

Lior Salem, Amir D. Gat and Yizhar Or are also with the Technion Autonomous Systems Program, Technion - Israel Institute of Technology, Technion City, Haifa, Israel 3200003.

This concept was used by many researchers for either grasping and manipulation [12], [13], actuation of rigid parts to create hybrid (soft-rigid) walking robots [14], [15], creating locomotion in passive elastic structures [16], or completely soft robots capable of walking (or swimming) locomotion [17], [18], [19]. All of the examples above are pneumatically actuated (hence often called Pneu-Nets) and require a tether to a fixed source of compressed air. The untethered versions either consist of more rigid parts [20], has significantly larger dimension [21], or relies on an on-board chemical reaction to generate pressure [22], [23]. A notable exception is [24], which is powered hydraulically by a closed circulation of pressurized liquid in the EFN, resulting in untethered function without significant change of the mechanical design.

While few works analyse the mechanics of an EFN based actuator [22], [25], and few other suggest kinematic models for control [12], [14], [26], [27], the soft robotics field is dominated by either finite elements or empirical modeling, or a straight-forward experimental approach, achieving *quasitatic* locomotion. To the best of our knowledge, the first works to propose an analytical model for both the pressure field in a slender fluidic channel and the actuator's *dynamic* response are [28], [29]. These works presented a general formulation, yet analyzed solutions for specific limiting cases with either negligible viscosity of the fluid, or negligible inertial effect of the elastic beam.

The goal of this work is to complete previous studies [28], [29] by introducing an analytical general systematic solution scheme for an elastic actuator with slender EFN channel, that accounts for the coupled effects of the beam's inertia and elasticity with the fluid's viscosity. The results are confirmed by numerical analysis and compered to preliminary experimental results [30].

II. Problem Formulation

In this section we introduce the proposed configuration and the governing equations, as a brief review of [28], [29]. We consider the dynamics of a rectangular elastic beam (height h, width w and length L) with a slender serpentine channel network embedded at an offset from the beam's neutral plane (see Figure 1). The channel is considered to consist mostly of segments perpendicular to the longitudinal direction of the beam x, and distributed rather densely such that the segments parallel to x are insignificant. The Young's modulus, mass per unit length, cross-section area and second moment of area of the beam are E, ρ, A and I respectively, while the pressure within the the fluidic network is denoted as $p(x,t)$.

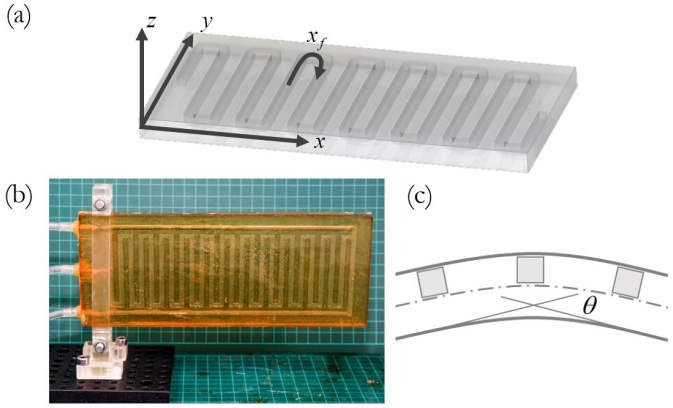

Fig. 1: Elastic beam with an embedded fluidic network (EFN) illustration and model.

In Section II-A the pressure field is assumed to be known and the governing equations of the elastic domain are introduced. The pressure field is later determined by the fluidic domain equations, introduced in Section II-B.

A. The Elastic Domain

Assuming small deformations, the deflection of the beam in the z direction, d, is composed of d_e, the beam dynamic response due to external forces, and d_p, the deflection due to the pressurized channel network,

$$d = d_e + d_p. \tag{1}$$

The EFN causes *local* strain in a field at an offset from the neutral plane, hence d_p can be considered as a kinematic slope constraint,which does not participate in the elastic term of the beam. However, the inertia and damping depend on the absolute displacement d. Such approach is often used in similar analysis in the field of Poroelasticity [31], giving an Euler-Bernoulli equation of the form

$$EI\frac{\partial^4}{\partial x^4}d_e + c\frac{\partial}{\partial t}(d_e + d_p) + \rho A\frac{\partial^2}{\partial t^2}(d_e + d_p) = w(x,t), \tag{2}$$

where $w(x,t)$ is the external distributed force acting on the actuator, and c is the proportional damping, estimated from experiments. The assumption of small deformations is widely used for the linear approximation, and even when slightly violated gives important insights on the physics of the problem. Moreover, the experimental results introduced later are in good agreement for the range $p/E \approx 0.1$.

The change in the beam's slope due to a single pressurized channel is denoted as θ (see Figure 1(c)). For a given channel density function $\varphi(x)$, defined as number of channel segments per unit length, the distributed change in the slope due to the EFN, $\varphi(x)\theta$, is proportional to the second derivative of the deflection d_p. The change in the beam's slope for a unit normalized pressure is denoted by λ, which is constant for each actuator, and is found via static calibration experiments. This relates the beam deflection to the pressure in the EFN by

$$\frac{\partial^2 d_p}{\partial x^2} = -\varphi(x)\theta \approx -\varphi(x)\lambda\frac{p(x,t)}{E}. \tag{3}$$

This relation has been shown to be accurate for $p/E < 0.1$ in [28], but provides fair approximation for a larger range.

While the current analysis focuses on slender channel, a similar approach may be applied for configurations with large bladders. The coefficient λ will incorporate the difference.

From (1) and (3), the beam equation (2) is rewritten in terms of d_e, as

$$EI\frac{\partial^4 d_e}{\partial x^4} + c\frac{\partial d_e}{\partial t} + \rho A\frac{\partial^2 d_e}{\partial t^2} = w(x,t) + \\ + \frac{\lambda}{E}\left(\rho A\frac{\partial^2}{\partial t^2} + c\frac{\partial}{\partial t}\right)\int_0^x\int_0^\eta \varphi(\xi)p(\xi,t)d\xi\ d\eta. \tag{4}$$

Considering a clamped-free configuration with no external forces but the EFN gives the homogeneous boundary conditions

$$d_e(0,t) = \frac{\partial d_e}{\partial x}(0,t) = 0, \tag{5a}$$

and

$$EI\frac{\partial^2 d_e}{\partial x^2}(L,t) = EI\frac{\partial^3 d_e}{\partial x^3}(L,t) = 0. \tag{5b}$$

Introducing nondimensional parameters $X = x/L$, $D_e = d_e/h$, $P = p/E$ and $T = \Omega t$, where $\Omega = \sqrt{EI/\rho AL^4}$ is the characteristic frequency, the elastic beam governing equation (4) becomes

$$\frac{\partial^4 D_e}{\partial X^4} + 2\zeta\frac{\partial D_e}{\partial T} + \frac{\partial^2 D_e}{\partial T^2} = W(X,T) + \frac{\lambda\varphi^* L^2}{h}\times \\ \times\left(\frac{\partial^2}{\partial T^2} + 2\zeta\frac{\partial}{\partial T}\right)\int_0^X\int_0^\eta \Phi(\xi)P(\xi,T)d\xi\ d\eta \triangleq F(X,T), \tag{6}$$

for $\Phi = \varphi/\varphi^*$ normalized channel density, where $\varphi^* = l/l_f L$ is the characteristic channel density, l is the total fluidic channel's length, l_f is the length of a single channel segment, and $\zeta = c/2\Omega\rho A$ is the nondimensional damping ratio. The nondimensional external load $W = wL^4/EIh$, can be either distributed along the actuator, or a localized force of the form $F_0(T)\delta(X - X_0)$. The overall excitation of the actuator, which includes the external forces and the contribution of the EFN, is denoted by $F(X,T)$.

B. The Fluidic Domain

In order to determine the pressure distribution function $p(x,t)$ in (4), we consider the incompressible creeping Newtonian flow within the fluidic network in the channel's spatial coordinates (x_f, y_f, z_f), where x_f is in the streamwise direction. The fluid is governed by the the Stokes equations,

$$\mu\nabla^2\mathbf{u} = \nabla p(x_f,t) \tag{7}$$

and conservation of mass

$$\nabla \cdot \mathbf{u} = 0, \tag{8}$$

where $\mathbf{u} = (u, v, w)$ is the velocity field in the corresponding coordinates and μ is the fluid viscosity.

Assuming a rectangular channel with characteristic cross-section dimension h_f, cross-section area a and total length l, we introduce the normalized channel-spatial coordinates $(X_f, Y_f, Z_f) = (x_f/l, y_f/h_f, z_f/h_f)$. It is noted that while the excitation of the elastic beam, defined in (6), is of form $P(X, T)$, the pressure field is defined in the fluid coordinates as $P(X_f, T_f)$. Therefore, a transformation from the channel-spatial coordinate X_f to the beam longitudinal coordinate X is introduced as follows

$$X_f \approx \int_0^X \Phi(\xi) d\xi + \frac{L}{l} X, \tag{9}$$

and the time scaling transformation is calculated by

$$T/T_f \triangleq \tau. \tag{10}$$

For a slender channel, the channel's total length l is significantly greater than the cross-section dimension h_f, and the characteristic flow velocity in the stream-wise direction u^* is significantly greater than those perpendicular to the channel walls v^*, w^*, giving the small parameter $\varepsilon = h_f/l \sim v^*/u^* \sim w^*/u^*$. Considering that, nondimensional parameters are introduced as follows: $A = a/{h_f}^2$, $T_f = t/t_f^*$, $\mathbf{U} = (U, V, W) = (u/u^*, v/v^*, w/w^*)$ and $Q = q/{h_f}^2 u^*$, where q is the flow rate and $u^* = E\varepsilon^2 l/\mu$. The leading order of (7) is

$$\frac{\partial P}{\partial X_f} \sim \frac{\partial^2 U}{\partial Y_f^2} + \frac{\partial^2 U}{\partial Z_f^2}. \tag{11}$$

From (11) it is noticed that the normalized flow rate Q, can be represented by

$$Q(X_f, T_f) = -Q_1 \frac{\partial P}{\partial X_f}(X_f, T_f), \tag{12}$$

where Q_1 is a constant determined by the channel's geometry, via solving (11) for a unit pressure gradient $\partial P/\partial X_f = -1$. For a rectangular cross-section of normalized length 1, this gives $Q_1 \approx 0.035$.

Assuming uniform cross-section area at rest and requiring small displacements, the cross-section can be approximated as $A(X_f, T_f) \approx 1 + A_P \; P(X_f, T_f)$. The coefficient A_P can be measured by calibration experiments. The leading order of the mass conservation equation (8) in its integral form, while considering (12), gives the flux continuity equation

$$-\frac{\partial^2 P}{\partial X_f^2} + \frac{\partial P}{\partial T_f} = 0, \tag{13}$$

which defines the characteristic time as $t_f^* = \mu A_P / Q_1 E \varepsilon^2$.

Considering the fact that the deflection will change the effective pressure in the channel, the problem will become two-way coupled. It can be shown [29] that since in our work the channel is slender, the change in the pressure due to loading is negligible compared to characteristic inlet pressures. This effect should be considered in the case of large bladders.

III. Analytical Solution Scheme

This section introduces a general analytical solution scheme for the presented governing equations (6,13) of the corresponding domains.

A. The Elastic Domain

The solution to the dynamic beam problem (6) excited by the EFN is represented by an infinite series of the mode-shape functions $\Psi_n(X)$ and time-varying magnitudes [32], [33], i.e.

$$D_e(X, T) = \sum_{n=1}^{\infty} A_n(T) \Psi_n(X). \tag{14}$$

The mode-shapes are determined from the eigenfunction problem corresponding to the homogeneous beam equation (6) (for $F(X, T) = 0$). For the clamped-free boundary conditions (5), this gives

$$\Psi_n(X) = \cosh(\alpha_n X) - \cos(\alpha_n X) + \\ + C_n \big(\sin(\alpha_n X) - \sinh(\alpha_n X) \big) \tag{15}$$

where $C_n = (\cos \alpha_n + \cosh \alpha_n)/(\sin \alpha_n + \sinh \alpha_n)$ and α_n are the solutions of the eigenvalue transcendental equation $\cosh \alpha_n \cos \alpha_n + 1 = 0$.

Putting (14) into (6), multiplying by each of the modes and integrating over the beam length, while considering the modes' orthogonality property, gives a series of ODEs in each of the magnitudes $A_n(T)$,

$$\ddot{A}_n(T) + 2\zeta \dot{A}_n(T) + {\alpha_n}^4 A_n(T) = \\ = \int_0^1 \Psi_n(X) F(X, T) dX \triangleq F_n(T), \tag{16}$$

where the natural frequencies are $\omega_n = {\alpha_n}^2$ and $\zeta < 1$. Solving these non-homogeneous linear ODEs gives the series solution for D_e of the form (14).

Finally, the total deflection $D = D_e + D_p$ is completed by calculating D_p from (3), as

$$D_p = -\frac{\lambda \varphi^* L^2}{h} \int_0^X \int_0^\eta \Phi(\xi) P(\xi, T) d\xi \; d\eta. \tag{17}$$

Hence, the second time derivative of the pressure field $\partial^2 P/\partial T^2$ excites the beam dynamic response D_e, while the "static" pressure P determines D_p, which can be considered as a quasistatic response to the kinematic constraint caused by the EFN.

B. The Fluidic Domain

The excitation $F(X,T)$, defined in (6), is a function of the pressure field $P(X,T)$, which is the solution of the diffusion equation (13) for known boundary conditions. Given a known inlet pressure $P_{in}(T_f)$ at one end of the channel, say from a pressure controller, while the other edge is sealed, so there is no flow and thus no pressure gradient. This gives the boundary conditions

$$P(0,T_f) = P_{in}(T_f), \tag{18a}$$

and

$$\frac{\partial P}{\partial X_f}(1,T_f) = 0. \tag{18b}$$

A correction function $W(X_f,T_f) = P(X_f,T_f) - P_{in}(T_f)$ is suggested in order to zero the boundary conditions, and equation (13) is reformulated in terms of W. Next, similarly to the solution scheme for the elastic domain, it is assumed that the non-homogeneous solution will be an infinite series of mode-shapes $\psi_m(X_f)$ multiplied by excitation-related time-varying magnitudes. Considering the correction function, this gives

$$P(X_f,T_f) = P_{in} + \sum_m B_m(T_f)\psi_m(X_f). \tag{19}$$

The pressure field mode shapes are obtained from the corresponding homogeneous problem as

$$\psi_m = \sin(\beta_m X_f), \tag{20}$$

for $\beta_m = \pi(2m-1)/2$. Putting (19) into (13), multiplying by each mode and integrating over the channel length gives a first-order ODE in each of the time-varying magnitudes

$$\dot{B}_m(T_f) + {\beta_m}^2 B_m(T_f) = -\frac{2}{\beta_m}\frac{\partial P_{in}}{\partial T_f}(T_f). \tag{21}$$

Defining the inlet as a gauge pressure, such that $P(X_f,0)=0$, solving (21) gives

$$B_m(T_f) = \\ = -\frac{2}{\beta_m}\exp\left(-{\beta_m}^2 T_f\right)\int_0^{T_f}\exp\left({\beta_m}^2\xi\right)\frac{\partial P_{in}}{\partial T_f}(\xi)d\xi. \tag{22}$$

Finally, substituting the modal magnitudes from (22) to (19) gives the general solution of the pressure field.

IV. Case Studies

This section studies several cases of interest in order to demonstrate the effects of viscosity, elasticity and inertia, and their interaction in soft actuators with EFN, without external loading $W(X,T)=0$.

A. The Effect of Viscosity – Step Inlet Pressure

To study how the viscosity of the fluid in the EFN affects the dynamic response of the beam, a step (Heaviside) pressure inlet of magnitude $\bar{P}$ is introduced, i.e. $P_{in}(T_f) = \bar{P}\,H(T_f)$. In this and the following sections we examine uniform channel distribution, $\Phi(X) = \bar{\Phi}$, hence the coordinates transformation in (9) is linear and can be denoted by a constant as $X_f = (\bar{\Phi} + L/l)X \triangleq C_\Phi X$.

From (19) and (22) the pressure field in the beam coordinates is

$$P(X,T) = \\ = \bar{P}H\left(\frac{T}{\tau}\right)\left[1 - \sum_{m=1}^{\infty}\frac{2}{\beta_m}e^{-T/\tau_m}\sin\left(\beta_m C_\Phi X\right)\right], \tag{23}$$

where $\tau_m = \tau/{\beta_m}^2$ is the m-th mode viscosity-dependent characteristic-time of the pressure field propagation.

The dynamic response D_e, is found by projection of the excitation on each of the modes, giving the modal excitation $F_n(T)$ from (16). Denoting the constants from the projection integrals for the n-th mode as

$$G_n = \frac{1}{2}\int_0^1 \Psi_n(X)X^2 dX, \tag{24a}$$

and

$$J_{n,m} = \\ = \frac{2}{{\beta_m}^2 C_\Phi}\int_0^1 \Psi_n(X)\left(\frac{\sin(\beta_m C_\Phi X)}{\beta_m C_\Phi} - X\right)dX, \tag{24b}$$

the time-dependent modal magnitudes are obtained from the solution of the linear ODE in (16). as

$$A_n(T) = \frac{\lambda\varphi^*\bar{\Phi}L^2}{h}\bar{P}\times \\ \times\left\{G_n\, e^{-\zeta T}\left[\cos(\omega_{nd}T) + \frac{\zeta}{\omega_{nd}}\sin(\omega_{nd}T)\right] + \right. \\ + \sum_{m=1}^{\infty}\frac{J_{n,m}}{{\tau_m}^2{\alpha_n}^4 - 2\tau_m\zeta + 1}\left[\tau_m{\alpha_n}^4 e^{-\zeta T}\left(\tau_m\cos(\omega_{nd}T) + \right.\right. \\ \left.\left. + \frac{\tau_m\zeta - 1}{\omega_{nd}}\sin(\omega_{nd}T)\right) + (1-2\tau_m\zeta)e^{-T/\tau_m}\right]\Bigg\}, \tag{25}$$

where $\omega_{nd} = \sqrt{{\alpha_n}^4 - \zeta^2}$.

The quasistatic response D_p is found from substituting (23) into (17) as

$$D_p(X,T) = -\frac{\lambda\varphi^*\bar{\Phi}L^2}{h}\bar{P}\left\{\frac{X^2}{2} + \right. \\ \left. + \sum_{m=1}^{\infty}\frac{2}{{\beta_m}^2 C_\Phi}\left[\frac{\sin(\beta_m C_\Phi X)}{\beta_m C_\Phi} - X\right]\exp\left(-\frac{T}{\tau_m}\right)\right\}, \tag{26}$$

giving the total beam deflection

$$D(X,T) = \sum_{n=1}^{\infty} A_n(T)\Psi_n(X) + D_p(X,T). \qquad (27)$$

Studying expression (26) shows that the quasistatic deformation D_p is similar in the time domain to a first-order system with characteristic time τ, where an exponential time delay accounts for the pressure propagation. From the solution of (16) the dynamic deformation's D_e time-dependent magnitudes $A_n(T)$, consist of exponentially decaying oscillating terms, which are similar to an impulse response of an under-damped second-order linear system.

The nondimensional time parameter τ represents the ratio between the fluidic viscous-elastic time scale and the beam's inertial-elastic characteristic time. We now turn to examine the limiting cases of τ. The pressure field of a fluid with negligible viscous effect propagates rapidly compared to the beam's characteristic response time ($\tau \ll 1$), hence the exponential delay in (23) vanishes. The overall response will resemble a step response of second-order under-damped linear system, as follows

$$D(X,T) = \frac{\lambda\varphi^*\bar{\Phi}L^2}{h}\bar{P}\Bigg\{ -\frac{X^2}{2} + \\ + \sum_{n=1}^{\infty} G_n\ e^{-\zeta T}\left[\cos(\omega_{nd}T) - \frac{\zeta}{\omega_{nd}}\sin(\omega_{nd}T)\right]\Psi_n(X)\Bigg\}. \qquad (28)$$

On the other hand, for viscous limit of $\tau \gg 1$ it can be shown that the dynamic beam deflection D_e vanishes, thus making the total deflection determined only by the constraint from the EFN, i.e. $D = D_p$ from (26). In this case the beam is considered to be in constant quasistatic equilibrium, and its response resembles an exponential rise without oscillations as of a first-order linear system. Some interesting cases of $\tau \gg 1$ are suggested in [29].

To study the interaction of the fluid viscosity and the beam inertial effects, fluids of various viscosities are considered. For concreteness, we consider the parameters of our experimental setup, summarized in Table I. These parameters give the characteristic time ratios as follows: for air $\tau \approx 10^{-4}$, for water $\tau \approx 10^{-2}$ and for glycerol $\tau \approx 10^{0}$. The step pressure inlet amplitude is 1 [bar] for all cases. The combined viscous-dynamic response of these fluids at the free end $X = 1$ is presented in Figure 2 (a,b,c). The analytical results (in solid grey line) are in excellent agreement with the numerical finite differences simulation (described in Appendix A), with maximal error of only 1.45% of the steady-state deformation (therefore the numerical results are not plotted in Figure 2). The comparison with the experimental results is discussed in the next section. As expected, the figure shows oscillations superimposed with an exponential rise to steady state. The first and even second natural frequencies are clearly recognized for air (from the faster oscillations over the basic harmonic) but become less significant as the viscosity increases. This phenomenon is explained by the frequency response analyses in the next section.

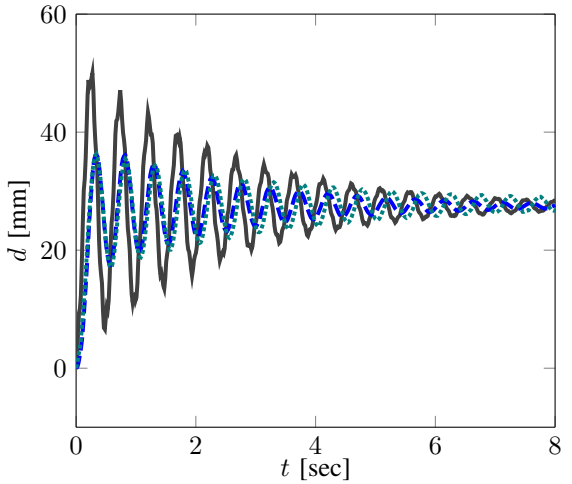

(a) Air-filled EFN actuator

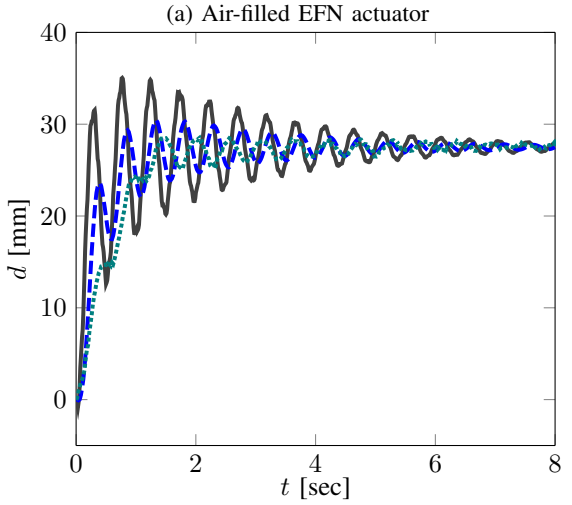

(b) Water-filled EFN actuator

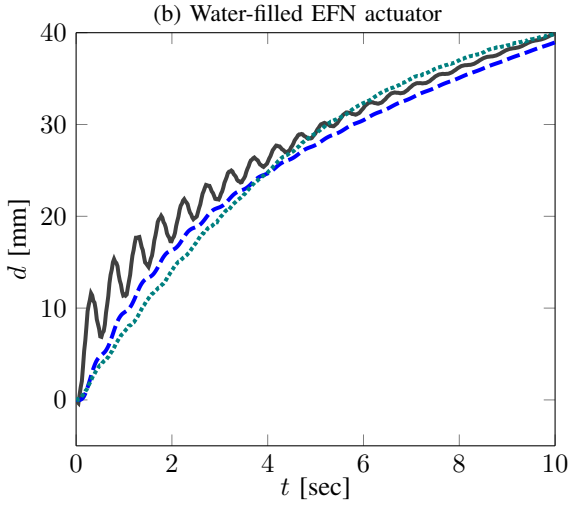

(c) Glycerol-filled EFN actuator

Fig. 2: Step response for different fluids at $X = 1$. Analytical step solution (solid grey), numerical "smoothed" inlet solution (dashed blue) and experimental results (dotted green)

.

Parameter	Notation	Value	Units
Young modulus	E	2	MPa
Beam density	ρ	1100	kg/m^3
Damping ratio	ζ	0.11	
Beam height	h	12	mm
Beam width	w	90	mm
Beam length	L	200	mm
Channel total length	l	3250	mm
Channel height	h_f	2	mm
Channel cross section area change for unit pressure	A_p	9.7	
Change in slope for unit pressure	λ	0.15	
Channel density	φ	25/L	1/mm
Air density order	μ_{air}	10^-5	Pa·s
Water density order	μ_{water}	10^-3	Pa·s
Glycerol density order	$\mu_{glycerol}$	10^0	Pa·s

TABLE I: Summary of experimental setup parameters' values

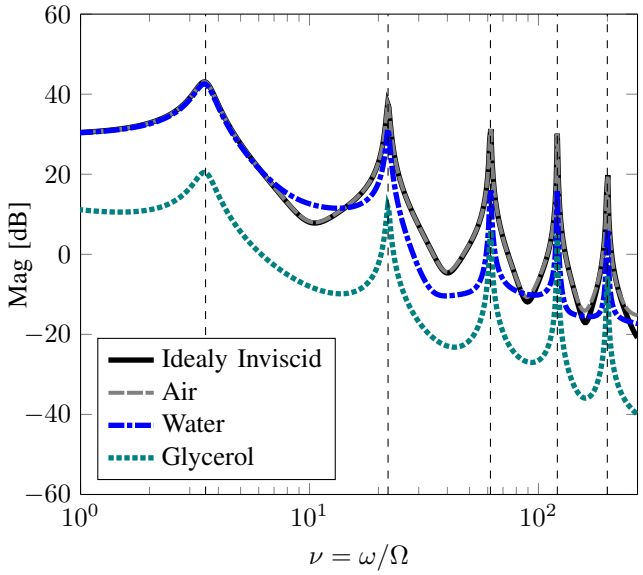

Fig. 3: Amplitude of FRF for liquids with various viscosities at $X = 1$. The analytical values of the resonance frequencies are marked by a vertical dashed line.

B. Frequency Response

To further study the dynamical effects and their coupling with the fluid's viscosity, this section analyses the frequency response function (*FRF*) of the beam under a harmonic pressure inlet in different fluids, i.e. $P_{in} = \bar{P}\exp(i\ \omega t_f^* T_f)$, where ω is the input frequency. This gives the expression for the pressure in steady-state as

$$P(X,T) = \\ = \bar{P}\left[1 - \sum_{m=1}^{\infty} \frac{2}{\beta_m} \frac{{\tau_m}^2\nu^2 + \tau_m\nu\ i}{{\tau_m}^2\nu^2 + 1} \sin(\beta_m C_\Phi X)\right] e^{(i\ \nu T)}, \tag{29}$$

where $\nu = \omega/\Omega$ is the normalized excitation frequency.

Since the beam's dynamics is linear and asymptotically stable, its response reaches steady-state harmonic with the same frequency as the input, but with different magnitude and phase, i.e. $A_n = \bar{A}_n \exp(i\ \omega t_f^* T_f)$, where $\bar{A}_n \in \mathbb{C}$. Given that, the FRF is obtained by analyses similarly to the previous section as

$$\frac{\bar{A}_n}{\bar{P}}(\nu) = \frac{\lambda\varphi^*\bar{\Phi}L^2}{h}\left[G_n + \sum_{m=1}^{\infty} J_{n,m}\frac{{\tau_m}^2\nu^2 + \tau_m\nu\ i}{{\tau_m}^2\nu^2 + 1}\right] \\ \times \frac{-\nu^2 + 2\zeta\nu\ i}{{\alpha_n}^4 - \nu^2 + 2\zeta\nu\ i}. \tag{30}$$

The right-most term in this expression is a typical FRF of a under-damped second-order system with an acceleration input, and will result in resonance peaks. It is therefore clear that the resonance frequencies are not affected by the fluid's viscosity. On the other hand, the viscosity-dependent term (under the summation) acts as a low-pass filter (LPF) and attenuates the frequency response from a cutoff frequency which drops as the viscosity rises. The static deflection D_p is found from (17) by integrating the pressure from (29) as

$$\frac{D_p}{\bar{P}}(\nu, X) = -\frac{\lambda\varphi^*\bar{\Phi}L^2}{h}\left\{\frac{X^2}{2} + \right. \\ \left. \sum_{m=1}^{\infty} \frac{{\tau_m}^2\nu^2 + \tau_m\nu\ i}{{\tau_m}^2\nu^2 + 1} \frac{2}{{\beta_m}^2 C_\Phi}\left[\frac{\sin(\beta_m C_\Phi X)}{\beta_m C_\Phi} - X\right]\right\} \tag{31}$$

This expression also shows a behaviour of a LPF, but without the resonance terms, as expected. The amplitude of FRF of the total deflection $D = D_e + D_p$ at the free end $X = 1$ is shown in Figure 3. We observe that the resonance frequencies are unchanged by the fluid, as expected, but the anti-resonances are somewhat smoothed. The whole FRF becomes more attenuated as the viscosity increases, which explains the attenuation of the oscillations in the step-responses in Section IV-A.

C. Inviscid Flow – Mode Elimination and Isolation

We now study the inviscid flow limit, with a general distribution of channels $\Phi = \Phi(X)$. We also emphasize that Φ may be positive or negative, representing that the channels are distributed along either side of the neutral plane. As previously discussed, in the inviscid limit of $\tau \ll 1$ the pressure field propagates much faster than the beam's inertial-elastic response time. The beam in fact behaves as if responding to a spatially uniform time-varying pressure, i.e. $P(X,T) = P_{in}(T)$. In this case, the beam's dynamic deflection D_e modal excitation becomes

$$F_n(T) = \frac{d^2 P_{in}(T)}{dT^2}\int_0^1 \left[\Psi_n(X)\int_0^X\int_0^\eta \Phi(\xi)d\xi\ d\eta\right] dX. \tag{32}$$

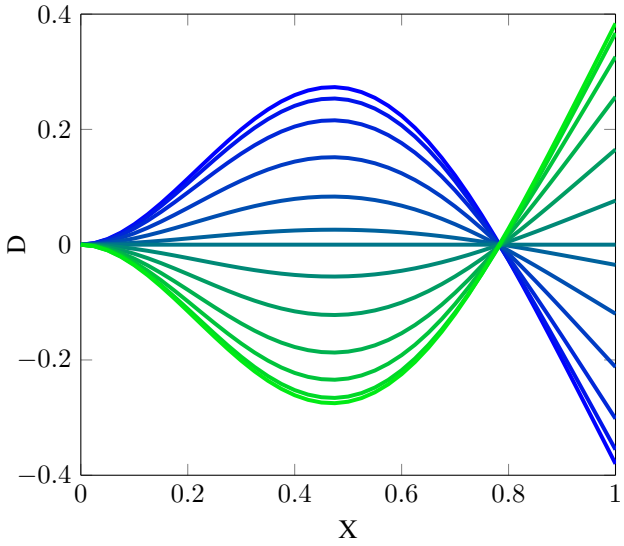

(a) Time snapshots of the beam's response to impulse from finite differences

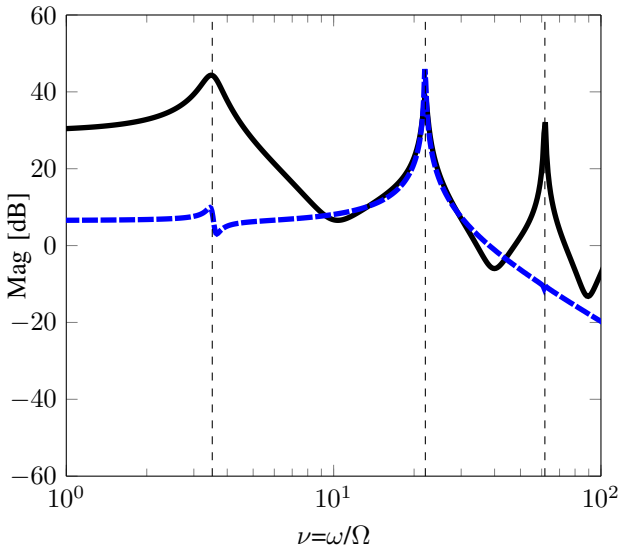

(b) FRF of a beam with second mode isolation (dashed blue line) compared to uniform channel distribution (solid black line) from finite differences

Fig. 4: Numerical demonstration of mode isolation

Therefore, if the second integral of the channel density function $\Phi(X)$ is orthogonal to a certain mode shape $\Psi_n(X)$, this mode is not excited for any inlet pressure. For example, when the first mode is eliminated this way, the beam's vibration is dominated by higher order mode-shapes and natural frequencies. Moreover, choosing channel density of the form $\Phi(X) = \Psi_k''(X)$ isolates only the k-th mode while all other modes do not appear in the response, since they are

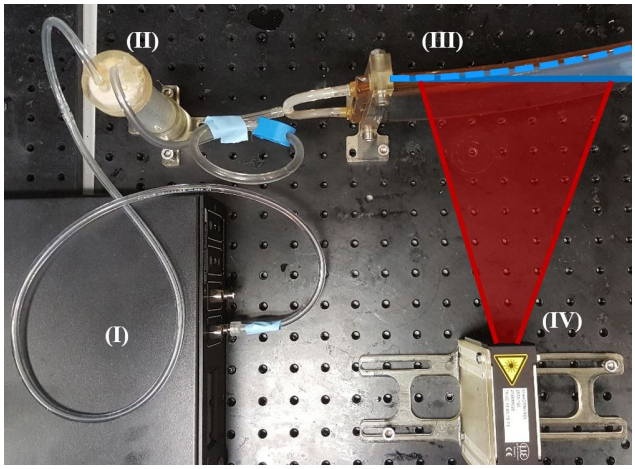

Fig. 5: Experimental setup – (I) Elveflow® pressure controller, (II) fluid reservoir, (III) cantilevered EFN beam, (IV) scanCONTROL laser profile sensor

orthogonal to the excitation distribution. This is valid for any input at any frequency. Figure 4a shows time snapshots of the beam's spatial response to an impulse pressure inlet (approximated by a bump function), obtained by a numerical simulation, where the channel distribution isolates the second mode $\Phi(X) = \Psi_2''(X)$. As expected, the response has the shape and natural frequency of the second mode *only*, unlike the response of a beam with uniform channel distribution, which has dominant first-mode shape and frequency (with some higher modes and harmonics slightly observed). The FRF of a beam with second mode isolation in Figure 4b shows that the other modes are attenuated even when the beam is excited at their natural frequency. The slight resonance peak observed at the first natural frequency, which is a result of the numerical discretization, implies that practical applications are limited, since in practice the channel distribution $\Phi(X)$ is implemented as a discrete function.

V. Experiments

The purpose of this section is to experimentally demonstrate the concepts introduced and analysed in this work. An elastic beam with EFN has been manufactured from a polymeric material (Econ® 60), having the properties mentioned in Table I. The transverse deflection direction Z has been positioned perpendicular to gravity in order to eliminate additional forces. Elveflow® OB1 MK3 pressure controller has been used in order to impose the prescribed pressure inlet function. Since this controller can only pressurize air, when working with other fluids a pressurised fluid reservoir has been installed, as shown in Figure 5. The beam deflection has been measured by Micro-Epsilon scanCONTROL 2650-100 laser profile sensor at sampling frequency of 30 [Hz]. The laser has been positioned such that it measures a range of $0.4 \leq X \leq 1$ of the beam's length with spacing of ~ 0.2 [mm] and accuracy of 12 [μm]. The measured data has been fitted at each time sample using least squares [34], in order to eliminate noise from various

factors which affect the laser reflectiveness, such as the beam's surface roughness.

To test the step inlet analysis in section IV-A, a *reverse step* experiment has been conducted [30]. In this experiment, in order to eliminate the effect of the controller's response time, the fluid has been pressurized to 1 [bar] until the beam deflection reached steady state, and then manually rapidly released. The measured dynamic response of the beam free end for various fluids is shown in Figure 2 in dotted green line. Qualitative comparison to the solutions obtained from the analytical model (solid grey line) shows similar behaviour of decaying oscillations superimposed on an exponential rise to steady state. On the other hand, it is obvious that the analytical Heaviside step pressure inlet cannot be implemented in practice. We hence also introduce a solution to a "smoothed" inlet of the form $P_{in} = 1-\exp(T/\delta)$, where δ is a small parameter. The resulting response (in dashed blue line), obtained from finite differences simulation, show excellent agreement with the experiments. Same result can be found from the analytical model, but the expressions are cumbersome and not shown. In all the case the linear damping model was found to be slightly inaccurate, which explains the differences in the decay form and the absence of the second oscillatory mode in the experiments, though was theoretically expected. Studies of the viscoelastic behaviour of polymers [35] suggest more complex modeling of the damping and stiffness coefficients is required in order to eliminate these errors, which is beyond the scope of this work. Discrete Fourier transform (DFT) analysis [36] of the reverse step responses show that the first natural frequency for all fluids has maximal error of only 8% compared to the analytical estimation, as expected from the FRF analyses. The error of the steady state amplitude is about 13%, which is explained by the nonlinear features of the material which are not modeled.

The FRF analysis in section IV-B is tested by *stepped sine* method – that is by introducing a sine inlet pressure at discrete frequencies and measuring the output amplitude at steady state. The upper limit of the controller is ~ 3 [Hz], showing the first resonance frequency, as presented in Figure 6 for water-filled EFN beam, normalized by the peak amplitude. The resonance in the experiments is reached with only 3% error in the frequency and 17.7% error in the amplitude.

The experimental results, show good qualitative and quantitative agreement with the theoretical results in Section IV. In particular, the effects of fluid viscosity and the first resonance frequency are clearly captured. It is also obvious that the material exhibits some nonlinear viscoelastic behaviour which should incorporated into the damping.

VI. Concluding Discussion

This work has formulated the viscous-elastic-inertial problem governing the dynamics of an elastic beam with a slender embedded fluidic network channel. A closed-form solution has been presented by combining tools from the fields of fluid mechanics and dynamic vibrations. The system's step-response and FRF were proposed theoretically, verified numerically and demonstrated by experiments. Mode elimination and isolation techniques were theoretically proposed.

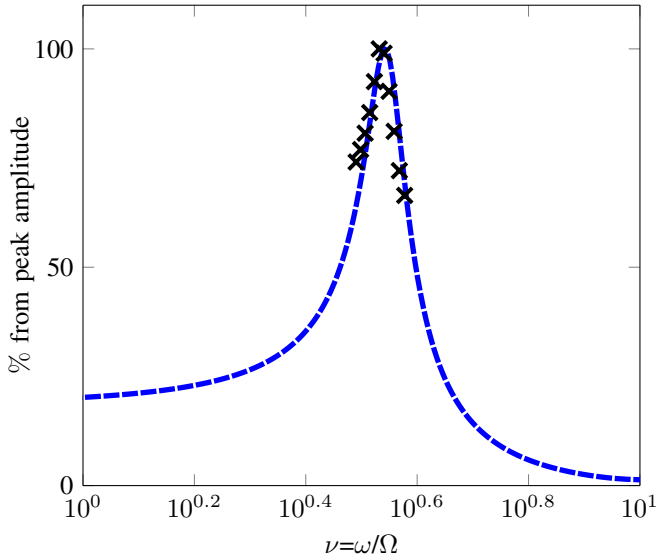

Fig. 6: Experimental demonstration of water FRF – stepped sine experiment (crosses) vs. analytical function (solid line) in percentage from peak amplitude

A major insight throughout this study is that the pressurised fluid in the channels, embedded into the elastic structure, simply acts as a distributed bending moment, leaving the beam's dynamical properties (such as resonance frequencies) unchanged. This observation allows for application of the presented analytical approach for similar cases of fluid-structure interaction.

Even though hydraulically powered EFN actuators have shown better untethered performance, researchers tend to avoid this actuation method due to viscous effects of liquids. We hope that this study sheds some light on the viscous-elastic-inertial behaviour of actuators for future design and control studies.

We now briefly discuss some limitations of our theoretical analysis and suggest possible directions for future extensions of the research. First, the proposed Euler-Bernoulli linear model accounts for small deformations, which is only relevant for some soft robotic configurations, especially quasistatic locomotion as [12], [17]. For configurations which require extremely large deflections nonlinear elasticity models must be employed. The study of such complicated models, as Elastica [25] and Cosserat [37], is only possible by numerical analysis. Yet for moderate displacements our experiments have shown reasonable agreement. Moreover, the range of applicability of the current analysis may be extended by asymptotic expansions for the limit of weak geometric nonlinearity, while maintaining the analytical insights.

Second, though the analysis for the elastic domain can also be applied in the case of large bladders (rather than a slender channel), while the difference is incorporated in the empirical coefficient λ, some key assumptions for the fluidic domain will be violated in that case, and a different formulation should be

presented.

Finally, the presented Euler-Bernoulli model can only account for transverse loading. Extending the model to include axial loading of the form $\gamma_n(X,T)$ will give the following governing equation

$$\frac{\partial^4 D_e}{\partial X^4}+\gamma_n\frac{\partial^2 D_e}{\partial X^2}+\frac{\partial \gamma_n}{\partial X}\frac{\partial D_e}{\partial X}+2\zeta\frac{\partial D_e}{\partial T}+\frac{\partial^2 D_e}{\partial T^2}= \frac{\lambda\varphi^* L^2}{h}\Big[\int_0^X\int_0^\eta \Phi(\xi)\frac{\partial^2 P(\xi,T)}{\partial T^2}d\xi\ d\eta+ +\frac{\partial \gamma_m}{\partial X}\int_0^X \Phi(\eta)P(\eta,T)d\eta+\gamma_n\ \Phi\ P(X,T)\Big]. \quad (33)$$

For the case of a constant normal force $\gamma_n(X,T)=\gamma_0$, there exist well known analytical solutions, which predict the shift in natural modes and frequencies and the buckling limit [33]. However, the case of an upright bipedal soft mechanism requires a complex solution for a general axial force, distributed in X and time-varying. This challenging problem is currently under investigation.

An extension of the presented model to include interaction between two (or more) beams with EFN, account for axial forces and changing boundary conditions due to contact transitions, is the immediate sequel to the study of soft robotic dynamic walking utilizing EFN actuators.

ACKNOWLEDGEMENT

This research was supported by the ISRAEL SCIENCE FOUNDATION (Grant No. 818/13), Technion Autonomous Systems Program (TASP) (Grant No. 2021779) and MAF'AT - Israel Ministry of Defense (Grant No. 2021845).

We thank Ms. Cathy Shih and Mr. Tsah Elimelech for conducting the experiments.

REFERENCES

[1] D. Trivedi, C. D. Rahn, W. M. Kier, I. D. Walker, Soft robotics: Biological inspiration, state of the art, and future research, Applied Bionics and Biomechanics 5 (3) (2008) 99–117.

[2] S. Kim, C. Laschi, B. Trimmer, Soft robotics: a bioinspired evolution in robotics, Trends in Biotechnology 31 (5) (2013) 287–294.

[3] D. Rus, M. T. Tolley, Design, fabrication and control of soft robots, Nature 521 (7553) (2015) 467–475.

[4] A. D. Marchese, R. K. Katzschmann, D. Rus, A recipe for soft fluidic elastomer robots, Soft Robotics 2 (1) (2015) 7–25.

[5] A. OHalloran, F. Omalley, P. McHugh, A review on dielectric elastomer actuators, technology, applications, and challenges, Journal of Applied Physics 104 (7) (2008) 071101.

[6] Y. Sugiyama, S. Hirai, Crawling and jumping by a deformable robot, The International Journal of Robotics Research 25 (5-6) (2006) 603–620.

[7] H. Jin, E. Dong, G. Alici, S. Mao, X. Min, C. Liu, K. Low, J. Yang, A starfish robot based on soft and smart modular structure (sms) actuated by sma wires, Bioinspiration & Biomimetics 11 (5) (2016) 056012.

[8] R. Cieslak, A. Morecki, Elephant trunk type elastic manipulator-a tool for bulk and liquid materials transportation, Robotica 17 (01) (1999) 11–16.

[9] M. Calisti, M. Giorelli, G. Levy, B. Mazzolai, B. Hochner, C. Laschi, P. Dario, An octopus-bioinspired solution to movement and manipulation for soft robots, Bioinspiration & Biomimetics 6 (3) (2011) 036002.

[10] C.-P. Chou, B. Hannaford, Measurement and modeling of McKibben pneumatic artificial muscles, IEEE Transactions on Robotics and Automation 12 (1) (1996) 90–102.

[11] B. Tondu, S. Ippolito, J. Guiochet, A. Daidie, A seven-degrees-of-freedom robot-arm driven by pneumatic artificial muscles for humanoid robots, The International Journal of Robotics Research 24 (4) (2005) 257–274.

[12] K. Suzumori, S. Iikura, H. Tanaka, Development of flexible microactuator and its applications to robotic mechanisms, in: Robotics and Automation, 1991. Proceedings., 1991 IEEE International Conference on, IEEE, 1991, pp. 1622–1627.

[13] F. Ilievski, A. D. Mazzeo, R. F. Shepherd, X. Chen, G. M. Whitesides, Soft robotics for chemists, Angewandte Chemie 123 (8) (2011) 1930–1935.

[14] K. Suzumori, Elastic materials producing compliant robots, Robotics and Autonomous Systems 18 (1) (1996) 135–140.

[15] C. D. Onal, D. Rus, Autonomous undulatory serpentine locomotion utilizing body dynamics of a fluidic soft robot, Bioinspiration & Biomimetics 8 (2) (2013) 026003.

[16] K. Suzumori, S. Endo, T. Kanda, N. Kato, H. Suzuki, A bending pneumatic rubber actuator realizing soft-bodied manta swimming robot, in: Proceedings 2007 IEEE International Conference on Robotics and Automation, IEEE, 2007, pp. 4975–4980.

[17] R. F. Shepherd, F. Ilievski, W. Choi, S. A. Morin, A. A. Stokes, A. D. Mazzeo, X. Chen, M. Wang, G. M. Whitesides, Multigait soft robot, Proceedings of the National Academy of Sciences 108 (51) (2011) 20400–20403.

[18] M. Wehner, R. L. Truby, D. J. Fitzgerald, B. Mosadegh, G. M. Whitesides, J. A. Lewis, R. J. Wood, An integrated design and fabrication strategy for entirely soft, autonomous robots, Nature 536 (7617) (2016) 451–455.

[19] A. D. Marchese, C. D. Onal, D. Rus, Autonomous soft robotic fish capable of escape maneuvers using fluidic elastomer actuators, Soft Robotics 1 (1) (2014) 75–87.

[20] A. A. Stokes, R. F. Shepherd, S. A. Morin, F. Ilievski, G. M. Whitesides, A hybrid combining hard and soft robots, Soft Robotics 1 (1) (2014) 70–74.

[21] M. T. Tolley, R. F. Shepherd, B. Mosadegh, K. C. Galloway, M. Wehner, M. Karpelson, R. J. Wood, G. M. Whitesides, A resilient, untethered soft robot, Soft Robotics 1 (3) (2014) 213–223.

[22] C. D. Onal, X. Chen, G. M. Whitesides, D. Rus, Soft mobile robots with on-board chemical pressure generation, in: International Symposium on Robotics Research, 2011, pp. 1–16.

[23] A. Wada, H. Nabae, T. Kitamori, K. Suzumori, Energy regenerative hose-free pneumatic actuator, Sensors and Actuators A: Physical 249 (2016) 1–7.

[24] R. K. Katzschmann, A. D. Marchese, D. Rus, Hydraulic autonomous soft robotic fish for 3d swimming, in: Experimental Robotics, Springer, 2016, pp. 405–420.

[25] K. M. de Payrebrune, O. M. O'Reilly, On constitutive relations for a rod-based model of a pneu-net bending actuator, Extreme Mechanics Letters 8 (2016) 38–46.

[26] C. Majidi, R. F. Shepherd, R. K. Kramer, G. M. Whitesides, R. J. Wood, Influence of surface traction on soft robot undulation, The International Journal of Robotics Research 32 (13) (2013) 1577–1584.

[27] A. D. Marchese, D. Rus, Design, kinematics, and control of a soft spatial fluidic elastomer manipulator, The International Journal of Robotics Research (2015) 0278364915587925.

[28] Y. Matia, A. D. Gat, Dynamics of elastic beams with embedded fluid-filled parallel-channel networks, Soft Robotics 2 (1) (2015) 42–47.

[29] Y. Matia, T. Elimelech, A. D. Gat, Leveraging internal viscous flow

to extend the capabilities of beam-shaped soft robotic actuators, Soft Robotics 4 (2) (2017) 126–134.

[30] See supplemental video online.

[31] G. Cederbaum, L. Li, K. Schulgasser, Poroelastic structures, Elsevier, 2000.

[32] S. S. Rao, Vibration of continuous systems, John Wiley & Sons, 2007.

[33] B. Balachandran, E. B. Magrab, Vibrations, Cengage Learning, 2008.

[34] T. Söderström, P. Stoica, System identification, Prentice-Hall, Inc., 1988.

[35] J. D. Ferry, Viscoelastic properties of polymers, John Wiley & Sons, 1980.

[36] K. Shin, J. Hammond, Fundamentals of signal processing for sound and vibration engineers, John Wiley & Sons, 2008.

[37] F. Renda, V. Cacucciolo, J. Dias, L. Seneviratne, Discrete cosserat approach for soft robot dynamics: a new piece-wise constant strain model with torsion and shears, in: Intelligent Robots and Systems (IROS), 2016 IEEE/RSJ International Conference on, IEEE, 2016, pp. 5495–5502.

[38] R.-D. Richtmyer, K.-W. Morton, Difference methods for initial-value problems, Interscience, 1957.

[39] R. J. LeVeque, Finite difference methods for ordinary and partial differential equations: steady-state and time-dependent problems, Vol. 98, SIAM, Society for Industrial and Applied Mathematics, 2007.

APPENDIX

This section presents a general solution scheme using finite differences formulation for vibrations of a damped beam with EFN, expressed by (2). First, this expression is rewritten in terms of the total deflection d from (3) (instead of d_e as in (4)), and transferred to the nondimensional parameters introduced in Section II, where $D = d/h$, giving

$$\frac{\partial^4 D}{\partial X^4} + C\frac{\partial D}{\partial T} + \frac{\partial^2 D}{\partial T^2} = \\ = -\frac{\lambda\varphi^* L^2}{h}\frac{\partial^2}{\partial X^2}\Big[\Phi(X)P(X,T)\Big] \triangleq F_{XX}(X,T), \quad (34)$$

where $C = \sqrt{c^2L^4/\rho AEI}$, for proportional damping c.

For a known pressure field $P(X,T)$, the PDE solution can be approximated over a grid with spacing ΔX and time step ΔT. Introducing D_i^n as the approximate solution to the deflection D at $T = n\ \Delta T$ and $X = i\Delta X$, using *central approximation*[38], [39] gives an explicit differences scheme

$$\left(1 + C\frac{\Delta T}{2}\right) D_i^{n+1} = 2D_i^n - \left(1 - C\frac{\Delta T}{2}\right) D_i^{n-1} \\ - \Delta^2(D_{i+1}^n - 4D_{i+1}^n + 6D_i^n - 4D_{i-1}^n + D_{i-2}^n) + \\ + \Delta T^2 F_{XX}(i\Delta X, n\Delta T), \quad (35)$$

where $\Delta = \Delta T/\Delta X^2$, and the truncation error is $O(\Delta T^2) + O(\Delta X^2)$. Since the pressure field is solved independently, it does not add to this error. Moreover, though the damping affects the error growth, it does not affect the stability condition, hence, Von Neumann's analysis [38], [39] indicates that the solution is stable provided $\Delta \leqslant 1/2$.

The pressure field in (13) is solved by introducing an implicit scheme, utilizing *one-sided approximation*. This scheme is unconditionally stable, which is more convenient for the solution of pressure fields of fluids with various viscosities. This results in a solution of the form

$$\mathbf{P}^{n+1} = \mathbf{M}^{-1}\left(\mathbf{P}^n - \mathbf{N}\right) \quad (36)$$

where for the boundary conditions introduced in (18)

$$\mathbf{M} = \begin{bmatrix} 2k\Delta + 1 & -k\Delta & & 0 \\ -k\Delta & \ddots & \ddots & \\ & \ddots & & -k\Delta \\ 0 & & -k\Delta & 2k\Delta + 1 \end{bmatrix}, \\ \mathbf{P}^n = \begin{bmatrix} P_1^n \\ \vdots \\ P_{1/\Delta X}^n \end{bmatrix},\ \mathbf{N} = \begin{bmatrix} -k\Delta P_{in}\big((n+1)\Delta T\big) \\ 0 \\ \vdots \\ 0 \end{bmatrix} \quad (37)$$

Here, though the pressure field is denoted by the same grid as the beam, for simplicity, its solution is actually attained in the channel-spatial coordinate X_f. A transformation is required, as described in Section II-B.